New Journal of Physics

The open access journal at the forefront of physics

PAPER

CrossMark

Strong-field assisted extreme-ultraviolet lasing in atoms and molecules

Timm Bredtmann[1], **Serguei Patchkovskii**[1] and **Misha Yu Ivanov**[1,2,3]

[1] Max-Born-Institute, Max-Born-Strasse 2A, D-12489 Berlin, Germany
[2] Department of Physics, Imperial College London, South Kensington Campus, SW7 2AZ, London, United Kingdom
[3] Department of Physics, Humboldt University, Newtonstrasse 15, D-12489 Berlin, Germany

E-mail: Timm.Bredtmann@mbi-berlin.de

Abstract

Using *ab-initio* simulations, we demonstrate amplification of extreme-ultraviolet (XUV) radiation during transient absorption in a high-harmonic generation type process using the example of the hydrogen atom. The strong IR driving field rapidly depletes the initial ground state while populating excited electronic states through frustrated tunnelling, thereby creating a population inversion. Concomitant XUV lasing is demonstrated by explicit inclusion of the XUV seed in our simulations, allowing a thorough analysis in terms of this transient absorption setup. Possibilities for increasing this gain, e.g. through preexcitation of excited states, change of the atomic gain medium or through multi-center effects in molecules, are demonstrated. Our findings should lead to a reinterpretation of recent experiments.

1. Introduction

Ultra-short laser pulses in the extreme-ultraviolet (XUV) and x-ray region are central to push time-resolved laser spectroscopy to the next level, including e.g. molecular movies of chemical reactions and the imaging of electrons on their natural time scale [1–3]. High-order harmonic generation (HHG) is capable of producing such radiation in compact table-top setups with high repetition rates [1]. However, the main drawback of HHG sources is their low conversion efficiency. One option to address this challenge is to rely on phase matching, see e.g. [4–7]. Another way is the enhancement of HHG at the single atom/molecule level by enhancing the first step of the HHG process—ionization—seeding it with single attosecond pulses or pulse trains, see e.g. [8–12]. This parametric process relies on the phase stability between the XUV seed and the IR driver.

Recently, the last step of the HHG process—recombination—has become the focus of many experimental studies, exploring the possibility of stimulated recombination of a continuum electron with its parent ion in the presence of an existing HHG photon with suitable energy [13–17]. The exponential amplification associated with such a stimulated process would constitute a major improvement of HHG sources: on one hand, the exponential scaling of the macroscopic photon yield with particle density in the stimulated case could, under suitable experimental conditions, considerably surpass the quadratic increase in standard HHG, the latter being only achievable using sophisticated phase-matching techniques [4–7]. On the other hand, the favorable coherence properties from standard HHG as well as the non-resonant nature of the process, allowing the amplifier to operate over wide spectral regions, would be preserved.

Specifically, experiments using helium gas as gain medium report impressive parametric amplification between 150 and 350 eV. The reported gain (g) length (L) product of $g \times L = 9$ around 1 bar pressure corresponds to the small-signal amplification factor of $e^{g \times L} \approx 8100$ [13]. The follow-up experiments [14–16] and the joint theoretical and experimental study [17] also report parametric amplification of x-ray radiation up to 1 keV [14]. Furthermore, the theoretical studies [18–21] and the joint theoretical and experimental work [17] support the interpretation of the experiments [13–17] as parametric amplification.

However, the interpretation of such experiments as parametric amplification of high frequency radiation is open to a challenge [22–24]. Specifically, using a Maxwell–Schrödinger model, [22, 23] argue that the super-quadratic growth of the HHG signal with gas pressure under tight focusing conditions reported experimentally in [13] can be completely accounted for by the phase matching in the standard (coherent parametric) HHG. Moreover, [24] shows that the gain (amplification) reported theoretically at the single atom level in [17, 19–21], is indeed the opposite, i.e. XUV loss. This observation in turn undermines the interpretation of the experimental results [13, 17] as stimulated HHG at the single atom level. Hence, given the relevance of a high fluence table top source in the XUV/x-ray frequency range and the current debate in the literature, further quantitative exploration of the possibility of stimulated recombination in HHG is needed.

Standard (coherent parametric) HHG always coexists with possible stimulated HHG, with the experimental parameters ultimately determining which of the two processes might dominate the macroscopic emission. Hence, in order to disentangle these two processes, which are experimentally inevitably intertwined, we focus on the single atom response and calculate the XUV transient absorption spectrum, $S_{XUV}(\Omega; \Omega_{XUV})$, in the presence of a strong IR driving field. The absorption cross section for an XUV pulse with central frequency Ω_{XUV}, $CS_{XUV}(\Omega_{XUV})$, in the IR dressed system is then obtained by integrating the XUV transient absorption spectrum over all frequencies ([25] and section 2). Experimentally, the XUV radiation may be supplied either using an external source [14, 15] or it might be generated through the standard HHG process in the medium (self-seeded amplification) [13].

2. Methods and theory

For the atomic systems, we solve the full three dimensional time-dependent Schrödinger equation in the velocity gauge using the implementation described in [26]. For the hydrogen atom, this corresponds to the full non-relativistic solution at the single particle level. For the helium atom, we use the single active electron approximation using the model potential from [27]. For the HHe^{2+} dimer, we solve the time-dependent Schrödinger equation for fixed internuclear distance in the length gauge [28]. The laser pulses are linearly polarized along the internuclear axis, and the resulting cylindrical symmetry is exploited. In all cases, complex absorbing potentials are used [29], and convergence of the results with respect to the size of the simulation box is verified.

The electric field for each pulse is defined via the vector potential $A(t)$. Sine-squared functions are used for the envelopes of the vector potential and the carrier envelope phase is set to $\phi = \pi/2$ [30]. For the eight-cycle flat-top pulse (figures 1 and 2), a two-cycle raising (falling) edge was chosen.

For the calculation of the XUV transient absorption spectrum, the total wavefunction of the system is $\Psi(t) = \Psi_{IR}(t) + \Delta\Psi_{XUV}(t)$. Here $\Psi_{IR}(t)$ is the wavefunction of the IR dressed system and $\Delta\Psi_{XUV}(t)$ is the perturbation due to the weak XUV probe. The induced dipole moment is

$$\langle\Psi(t)|\hat{d}|\Psi(t)\rangle = \langle\Psi_{IR}(t)|\hat{d}|\Psi_{IR}(t)\rangle + \langle\Psi_{IR}(t)|\hat{d}|\Delta\Psi_{XUV}(t)\rangle + \langle\Delta\Psi_{XUV}(t)|\hat{d}|\Psi_{IR}(t)\rangle$$
$$+ \langle\Delta\Psi_{XUV}(t)|\hat{d}|\Delta\Psi_{XUV}(t)\rangle,$$
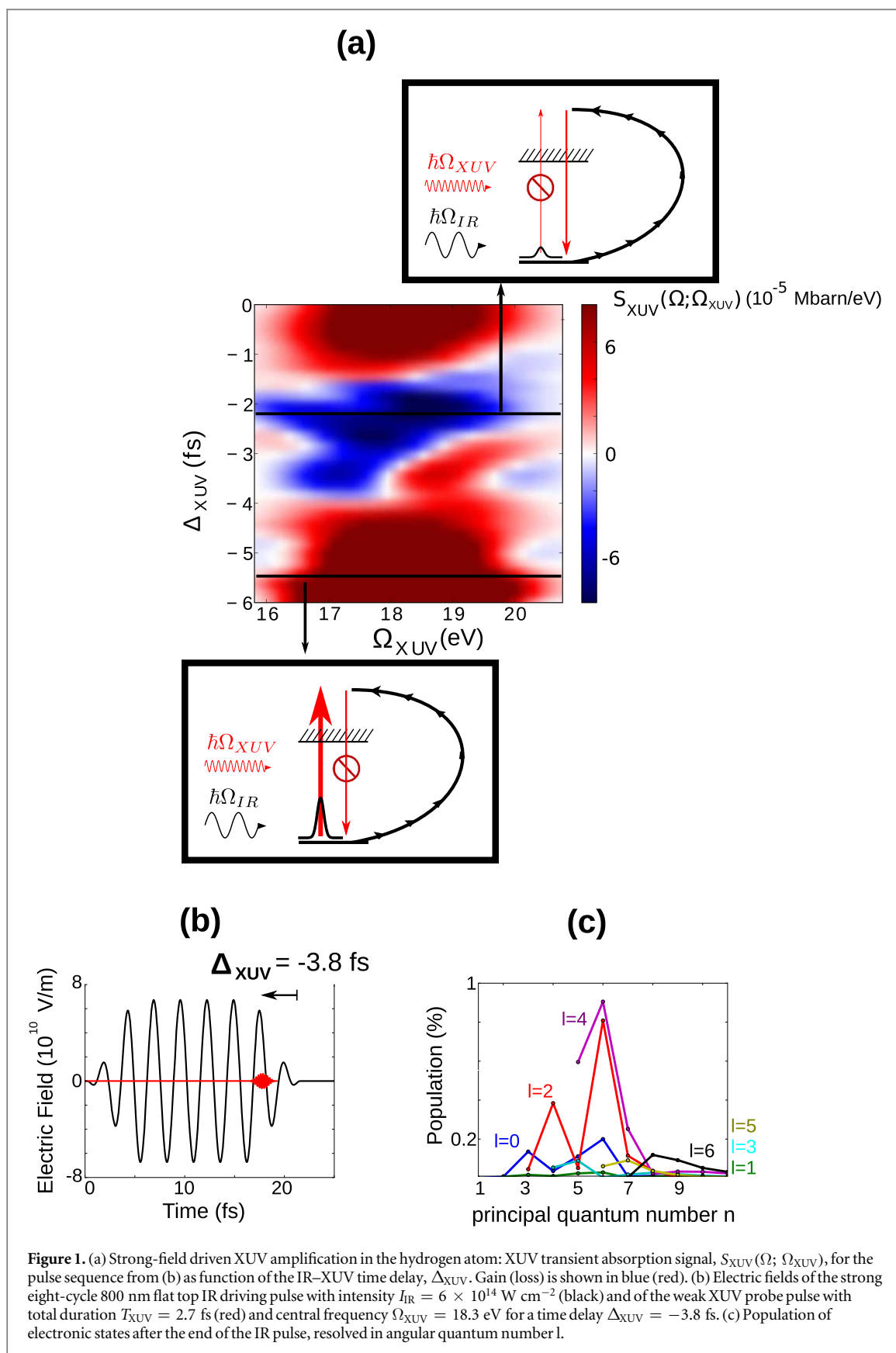
where $\hat{d}$ is the dipole operator. The first term on the right describes the nonlinear response to the strong IR field alone, without any assistance from the XUV. Thus, it does not include any XUV stimulated processes and contains only HHG-type emission during radiative recombination. The second and third terms describe XUV induced stimulated transitions in the IR dressed system, the subject of this paper. The last term depends quadratically on the weak XUV probe field and may thus be neglected for sufficiently low XUV intensities. In all calculations, the intensity of the XUV pulse is set to $I_{XUV} = 5 \times 10^{12}$ W cm^{-2}, which was tested to give stable numerical results while being in the linear response regime. For increased numerical stability, we use the dipole accelerations $a(t) = -\langle\Psi(t)|[H, [H, \mathbf{r}]]|\Psi(t)\rangle$ and $a_{IR}(t) = -\langle\Psi_{IR}(t)|[H, [H, \mathbf{r}]]|\Psi_{IR}(t)\rangle$, where $\mathbf{r}$ denotes the electronic coordinate.
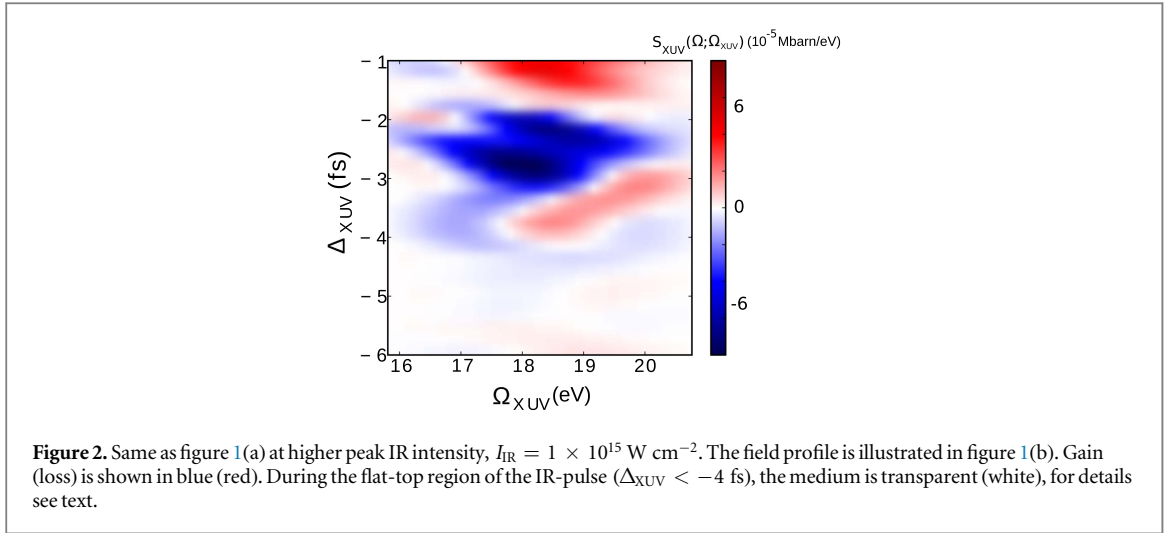
Hence, to identify XUV induced stimulated transitions, we calculate the frequency resolved linear response of the IR dressed system to the XUV probe pulse as

$$D_{XUV}(\Omega; \Omega_{XUV}) = \frac{1}{\Omega^2}\int dt e^{i\Omega t}(a(t) - a_{IR}(t)), \tag{1}$$

thereby removing the contribution of the standard HHG-type emission. Here, Ω_{XUV} denotes the central frequency of the XUV pulse and the numerical propagation is carried out until the end of the XUV probe pulse.

The XUV probe absorption/emission is determined by the relative phases of the XUV probe pulse, $E_{XUV}(\Omega; \Omega_{XUV})$, and the linear dipole response in the IR-dressed system, $D_{XUV}(\Omega; \Omega_{XUV})$. If both $E_{XUV}(\Omega; \Omega_{XUV})$ and $D_{XUV}(\Omega; \Omega_{XUV})$ are in phase, the IR-dressed medium is transparent to the XUV radiation. However, if there is a phase shift between $E_{XUV}(\Omega; \Omega_{XUV})$ and $D_{XUV}(\Omega; \Omega_{XUV})$, energy from the XUV field is absorbed (dipole response lags the electric field) or emitted (dipole response is in advance of the electric field)

Figure 1. (a) Strong-field driven XUV amplification in the hydrogen atom: XUV transient absorption signal, $S_{XUV}(\Omega; \Omega_{XUV})$, for the pulse sequence from (b) as function of the IR–XUV time delay, Δ_{XUV}. Gain (loss) is shown in blue (red). (b) Electric fields of the strong eight-cycle 800 nm flat top IR driving pulse with intensity $I_{IR} = 6 \times 10^{14}$ W cm^{-2} (black) and of the weak XUV probe pulse with total duration $T_{XUV} = 2.7$ fs (red) and central frequency $\Omega_{XUV} = 18.3$ eV for a time delay $\Delta_{XUV} = -3.8$ fs. (c) Population of electronic states after the end of the IR pulse, resolved in angular quantum number l.

Figure 2. Same as figure 1(a) at higher peak IR intensity, $I_{IR} = 1 \times 10^{15}$ W cm^{-2}. The field profile is illustrated in figure 1(b). Gain (loss) is shown in blue (red). During the flat-top region of the IR-pulse ($\Delta_{XUV} < -4$ fs), the medium is transparent (white), for details see text.

[25]. Specifically, the frequency resolved XUV probe absorption signal is the ratio of the absorbed/emitted energy and the total incoming energy (Gaussian units)

$$S_{XUV}(\Omega; \Omega_{XUV}) = \frac{2\Omega_{XUV} \, \mathrm{Im}(E_{XUV}^*(\Omega; \Omega_{XUV}) D_{XUV}(\Omega; \Omega_{XUV}))}{\frac{c}{2\pi} \int d\Omega |E_{XUV}(\Omega; \Omega_{XUV})|^2}, \tag{2}$$

where the refractive index is assumed to be 1 and c is the speed of light, see page 103, equations (4.89) and (4.90) in [25] and [24, 31, 32]. In all of the results presented here, positive (negative) values of $S_{XUV}(\Omega; \Omega_{XUV})$ correspond to XUV loss (gain).

The total XUV absorption cross section for central frequency Ω_{XUV} in the IR dressed system is obtained by integration over all positive frequencies [25], $\Omega > 0$,

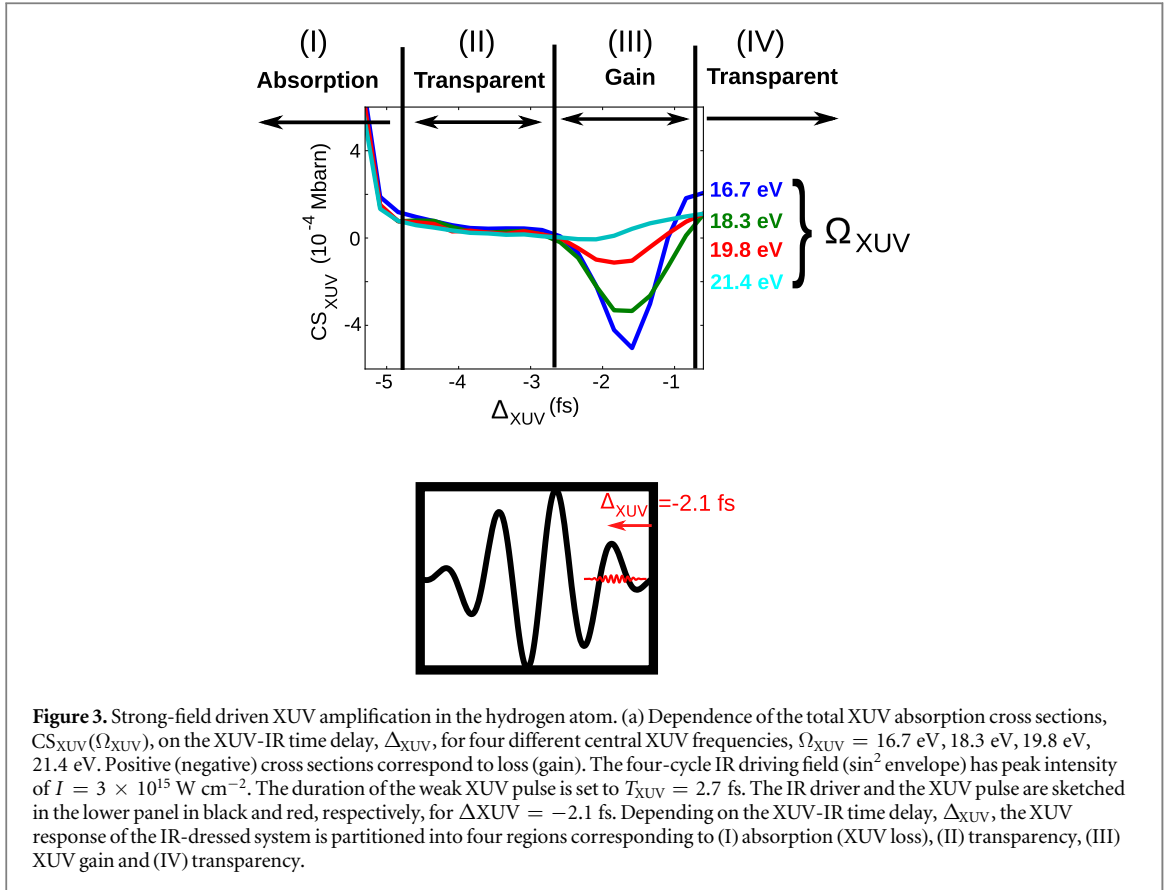$$CS_{XUV}(\Omega_{XUV}) = \int d\Omega \, S_{XUV}(\Omega, \Omega_{XUV}). \tag{3}$$

Positive (negative) values for the cross sections $CS_{XUV}(\Omega_{XUV})$ correspond to XUV loss (gain).

3. Results and discussion

Figure 1(a) shows the XUV transient absorption spectrum, $S_{XUV}(\Omega; \Omega_{XUV})$, in the IR dressed hydrogen atom as function of the time delay Δ_{XUV} between a strong ($I_{IR} = 6 \times 10^{14}$ W cm^{-2}) eight-cycle, 800 nm flat-top IR pulse and the weak XUV pulse with duration $T_{XUV} = 2.7$ fs and central frequency $\Omega_{XUV} = 18.3$ eV. Both pulses are shown in figure 1(b) for a time delay of $\Delta_{XUV} = -3.8$ fs, which is defined as the offset of the peak of the XUV envelope relative to the end of the IR pulse. Positive time delays correspond to non-overlapping pulses while negative time delays correspond to overlapping pulses. Note that the intensity of the weak XUV pulse is immaterial as long as it lies within the linear response regime, see section 2 for details. Experimentally, the XUV radiation may be supplied either using an external source [14, 15] or it might be generated through the HHG process in the medium (self-seeded amplification) [13].

Red (blue) colors in figure 1(a) correspond to XUV loss (gain). The two cartoons illustrate the loss and the gain mechanisms: For early time delays ($\Delta_{XUV} < -4$ fs), one photon absorption from the electronic ground state into the continuum is the main channel and leads to XUV loss dominating by far any possible stimulated process. In contrast, for $\Delta_{XUV} > -4$ fs we find evidence of stimulated recombination of the IR driven electron by the XUV field, i.e. XUV gain.
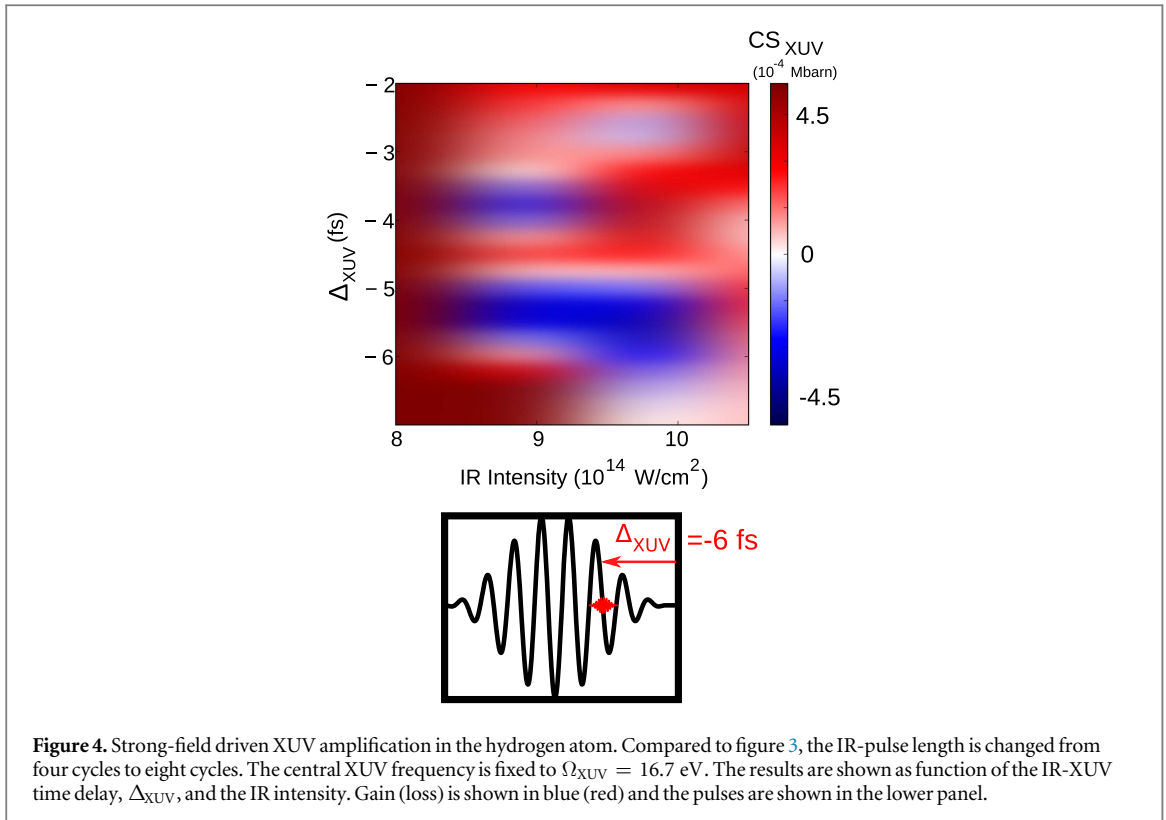
In this XUV gain process, the role of the strong IR driving field is two-fold: first, the IR field ionizes the medium, thereby suppressing XUV induced stimulated one-photon bound-free transitions by the ground state atoms, eliminating this parasitic loss channel once the ground state is fully depleted. This ionization process takes place over multiple laser cycles. Second, the IR field populates excited electronic states through frustrated tunneling [33–35]. These excited states experience stabilization and oscillate as a nearly free Kramers–Henneberger-like quasi-bound wavepacket in the IR driving field [31, 36–38]. XUV absorption by a nearly free electron to higher continuum states is far less likely than emission to the lowest, still well bound and now empty electronic states [28]. XUV amplification becomes possible once an inversion between these laser driven states and the electronic ground state is created. In this gain process, energy is transferred from the dressing IR to the weak XUV field. Figure 1(c) further illustrates this mechanism by showing the state resolved populations of the

Figure 3. Strong-field driven XUV amplification in the hydrogen atom. (a) Dependence of the total XUV absorption cross sections, $CS_{XUV}(\Omega_{XUV})$, on the XUV-IR time delay, Δ_{XUV}, for four different central XUV frequencies, $\Omega_{XUV} = 16.7$ eV, 18.3 eV, 19.8 eV, 21.4 eV. Positive (negative) cross sections correspond to loss (gain). The four-cycle IR driving field ($\sin^2$ envelope) has peak intensity of $I = 3 \times 10^{15}$ W cm^{-2}. The duration of the weak XUV pulse is set to $T_{XUV} = 2.7$ fs. The IR driver and the XUV pulse are sketched in the lower panel in black and red, respectively, for $\Delta XUV = -2.1$ fs. Depending on the XUV-IR time delay, Δ_{XUV}, the XUV response of the IR-dressed system is partitioned into four regions corresponding to (I) absorption (XUV loss), (II) transparency, (III) XUV gain and (IV) transparency.

electronic states after the end of the IR pulse. After the end of the IR pulse, the electronic ground state 1 s ($n = 1$, $l = 0$) is virtually empty while excited electronic states got populated up to close to 1%, with the highest population being in the states with high angular momenta, here the ($n = 6$, $l = 4$) state. While the IR field is still on, these dressed states are shifted energetically above the ionization threshold (I_p), which enables XUV lasing beyond I_p. The peak XUV absorption cross section, equation (3), occurs for IR-XUV time delay $\Delta_{XUV} = -2.2$ fs and is $CS_{XUV} (\Omega_{XUV} = 18.3$ eV$) = -1.4 \times 10^{-4}$ Mbarn.

Higher IR intensities lead to faster ionization of the ground state atoms. Consequently, one-photon absorption by the ground state (the cause of the XUV loss) is quenched already in the flat-top region of the IR pulse for higher IR intensities, see figure 2. Here, the peak intensity of the IR pulse is increased from $I_{IR} = 6 \times 10^{14}$ W cm^{-2} (figure 1) to $I_{IR} = 1 \times 10^{15}$ W cm^{-2}, while the remaining parameters are the same. Remarkably, XUV gain (blue) starts at virtually the same IR-XUV time delays as before (around $\Delta_{XUV} = -4$ fs), beyond the flat-top region. For these delays ($\Delta_{XUV} > -4$ fs), the IR intensity already dropped significantly, see figure 1(b). Hence, we observe that strong-field driven XUV lasing occurs at the falling edge of the IR pulse, beyond the flat-top region. In this region, the system is still dressed, enabling XUV lasing in the vicinity of the ionization potential. The peak XUV cross section, equation (3), occurs for IR-XUV time delay $\Delta_{XUV} = -2.3$ fs and is $CS_{XUV} (\Omega_{XUV} = 18.3$ eV$) = -1.9 \times 10^{-4}$ Mbarn, quite similar to the gain at lower IR intensities, figure 1.

We also explored a range of higher central XUV frequencies. No evidence of gain from strongly driven electrons with energies far beyond the ionization threshold during the flat-top region of the IR pulse could be seen (also see figure 3). These results are not unexpected: first, the photoionization cross section $\sigma(\Omega)$ falls off as $\Omega^{-7/2}$ [39]. Second, emission is only possible near the core, where the strongly driven electron spends a very small fraction of its time. In other words, the dressed states are spread out over a distance $\propto E_{IR}/\Omega_{IR}^2$ [1]. Third, the absorption cross section, $CS(\Omega)$, is proportional to the photoionization cross section, $\sigma(\Omega)$, times the differences in the populations of the dressed initial (ground state) and final (continuum) levels. In the flat-top region of the IR pulse, the electron is strongly driven, with the mean energy of U_p ($U_p = E_{IR}^2/4\Omega_{IR}^2$). Classically, its instantaneous kinetic energy varies from 0 to $2U_p$ [1]. For the parameters of figure 2 $U_p \approx 60$ eV. Consequently, the populations of the continuum states at any particular energy are only a fraction of the total continuum population. Because the ground state remains fractionally populated, the overall absorption cross section $CS(\Omega)$ becomes either positive (absorption of XUV) or very small (transparency). In contrast, in the parametric HHG process, the emission is proportional to the *product* of the same populations and the

Figure 4. Strong-field driven XUV amplification in the hydrogen atom. Compared to figure 3, the IR-pulse length is changed from four cycles to eight cycles. The central XUV frequency is fixed to $\Omega_{XUV} = 16.7$ eV. The results are shown as function of the IR-XUV time delay, Δ_{XUV}, and the IR intensity. Gain (loss) is shown in blue (red) and the pulses are shown in the lower panel.

photoionization cross section, so that the parametric HHG emission remains possible, as long as the ground state is not fully depletetd.

At the falling edge of the IR pulse, the continuum populations increase close to the ionization threshold I_p (due to the decrease in U_p). At the same time, the photoionization cross section $\sigma(\Omega)$ also increases. If the continuum populations exceed the residual ground state population, XUV amplification becomes efficient.

Concerning the synchronization of the pulses, amplification occurs for a range of IR-XUV time delays of about 1.5 fs, much longer than the XUV half cycle. Thus, phase matching carrier oscillations of the XUV-IR pair within one XUV half cycle, as in the parametric HHG process, is not required.

The strong-field assisted XUV lasing mechanism in the hydrogen atom is explored further in figure 3. The figure shows the XUV absorption cross sections, $CS_{XUV}(\Omega_{XUV})$ equation (3), as a function of the IR-XUV time delay, Δ_{XUV}. Positive (negative) absorption cross sections correspond to loss (gain). Here, the intensity ($I_{IR} = 3 \times 10^{15}$ W cm^{-2}), pulse shape (sin^2) and duration (four-cycle) of the IR driving field is changed compared to figures 1 and 2. Four different central XUV frequencies Ω_{XUV} are used (results shown in different colors). The pulses are shown in the lower panel.

Despite the very different parameters used here, the characteristics of the strong-field driven XUV amplification are virtually identical to the results presented in figures 1 and 2. In accordance with the mechanism described above, the dependence of the amplification on the IR-XUV time delay, Δ_{XUV}, can be divided into four regions indicated in the figure 3: (I) absorption by ground state atoms, (II) transparency when the ground state is depleted and the electron is strongly driven, (III) gain during the falling edge of the pulse, (IV) transparency for XUV frequencies beyond the ionization threshold when there is no more overlap of the IR and XUV pulses. Furthermore, the XUV amplification decreases gradually with increasing detuning of Ω_{XUV} from the ionization threshold, in agreement with the mechanism described above. Also, the absorption cross sections differ at most by a factor of 2 compared to figures 1 and 2, which underlines again the robustness of the results, given the very different laser parameters used for the IR driving field. In particular, CS (18.3 eV) $\approx -3 \times 10^{-4}$ Mbarn.

Figure 4 explores the dependence of the XUV amplification on the IR intensity, again as function of the IR-XUV time delay, Δ_{XUV}. Here, the central XUV frequency is set again to $\Omega_{XUV} = 16.7$ eV (previously shown as blue line in figure 3) and an eight-cycle IR driving field with sin^2-envelope is used (i.e. twice as long as in figure 3). Below an intensiy of $I_{IR} = 8 \times 10^{14}$ W cm^{-2} there is only XUV loss since there is still dominant XUV absorption from the ground state atoms. This intensity dependence shows the effect of the pulse shape: in figure 1, XUV lasing started at lower IR intensities ($I_{IR} = 6 \times 10^{14}$ W cm^{-2}). However, in the latter simulations, a flat-top pulse was used which depletes the electronic ground state more efficiently. Apart from this shift to higher intensities, the characteristics of XUV lasing, in particular the associated absorption cross sections and the
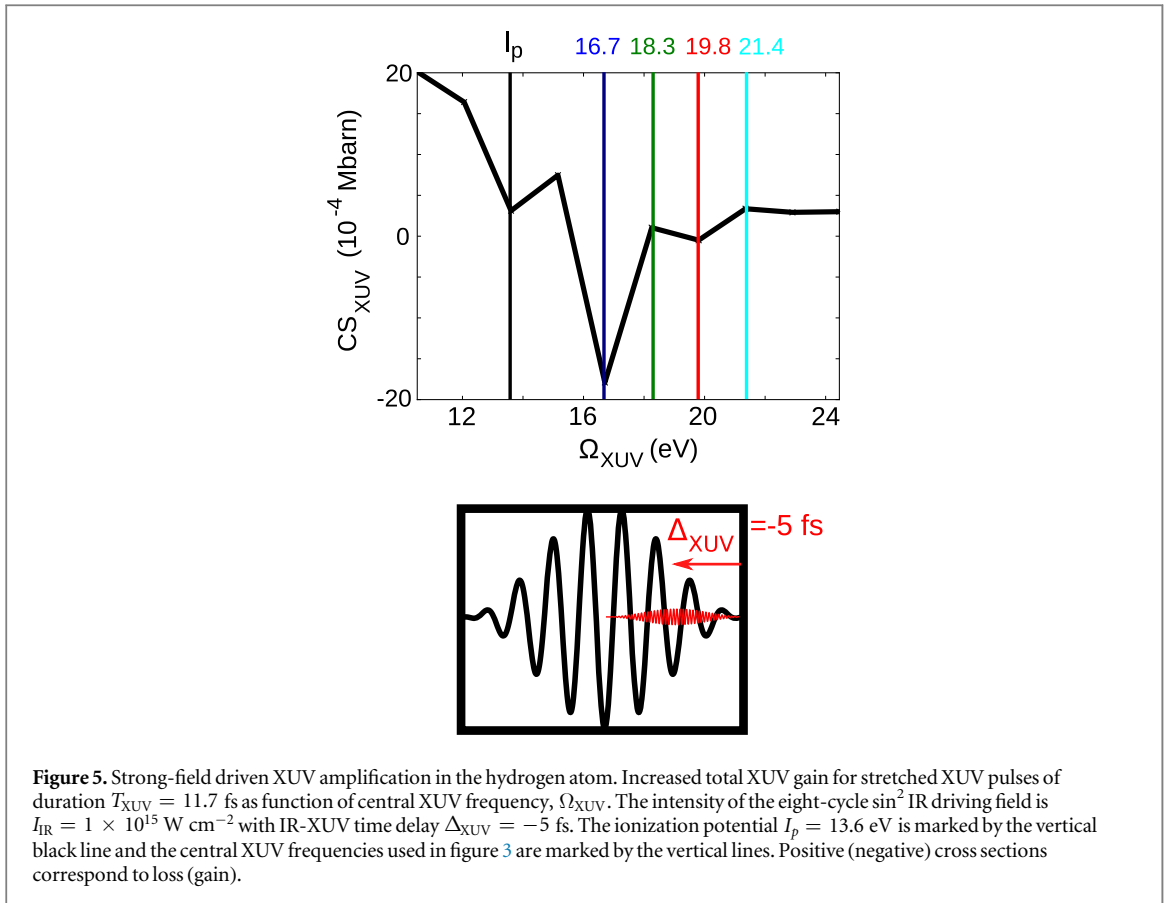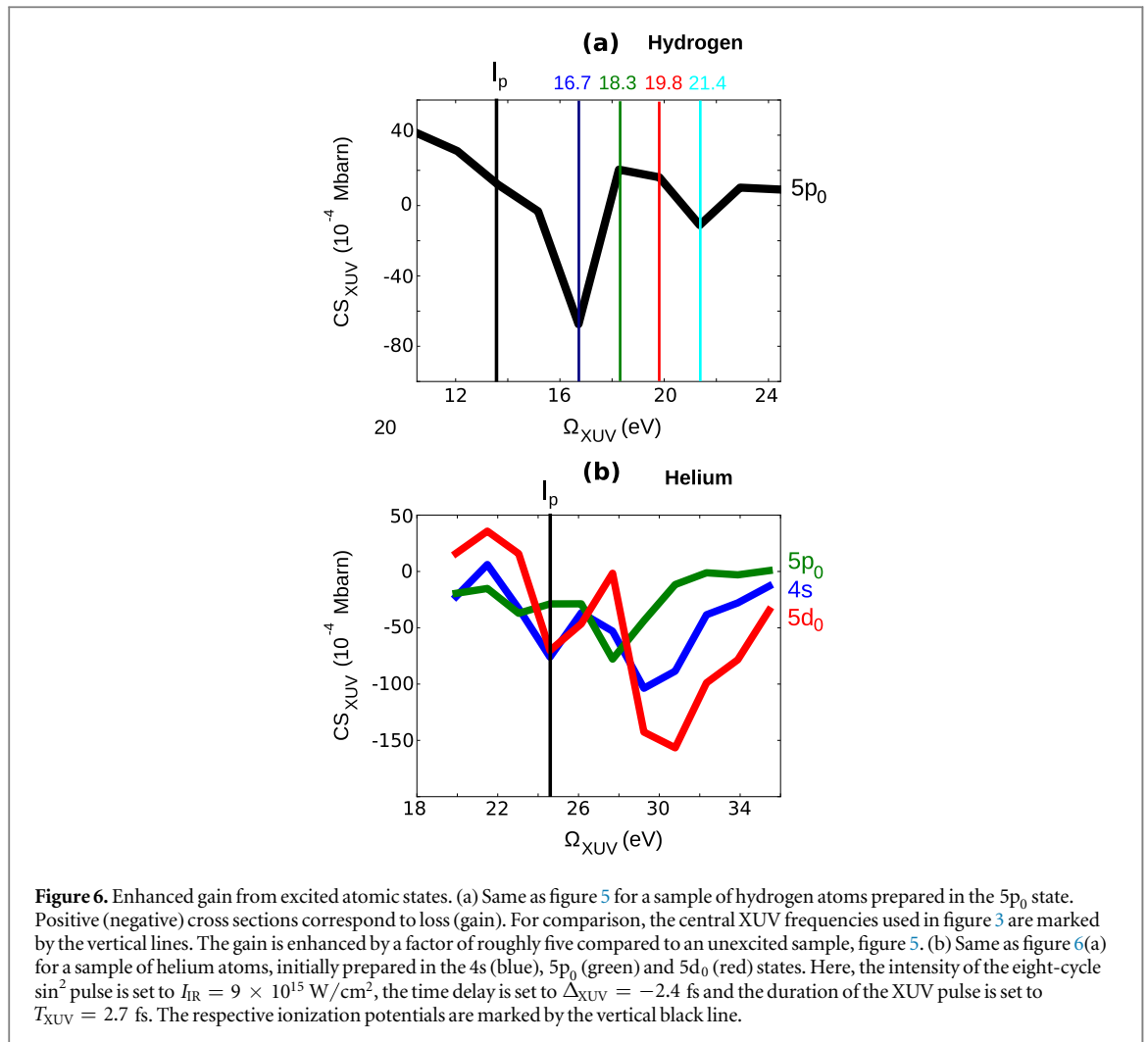
Figure 5. Strong-field driven XUV amplification in the hydrogen atom. Increased total XUV gain for stretched XUV pulses of duration $T_{XUV} = 11.7$ fs as function of central XUV frequency, Ω_{XUV}. The intensity of the eight-cycle $\sin^2$ IR driving field is $I_{IR} = 1 \times 10^{15}$ W cm^{-2} with IR-XUV time delay $\Delta_{XUV} = -5$ fs. The ionization potential $I_p = 13.6$ eV is marked by the vertical black line and the central XUV frequencies used in figure 3 are marked by the vertical lines. Positive (negative) cross sections correspond to loss (gain).

dependence on the IR-XUV delay are again very similar to the results above. In particular, the peak cross section around $\Delta_{XUV} = -5$ fs is $CS_{XUV} (\Omega_{XUV} = 16.7$ eV$) = -4.5 \times 10^{-4}$ Mbarn, virtually identical to the results shown in figure 3. Of course, in figure 3 higher intensities had to be used due to the shorter IR-pulse duration.

Again, with increased IR intensity XUV lasing occurs at earlier times (smaller time delays Δ_{XUV}) since the ground state gets depleted more rapidly. However, too strong IR fields suppress the XUV lasing, due to rapid, complete ionization not only from the ground state, but also from the excited states that act as inverted medium.

Finally, figure 5 explores XUV lasing for stretched XUV pulses ($T_{XUV} = 11.7$ fs, see lower panel for a sketch of the pulses). XUV pulse reshaping is likely to occur during propagation of the fields through the atomic medium. The parameters chosen for the IR pulse allow comparison to figure 4, where the peak cross section was $CS_{XUV} (16.7$ eV$) = -4.5 \times 10^{-4}$ Mbarn. We observe that for stretched XUV pulses, the amplification is enhanced by a factor of roughly 4. Increasing the length of the XUV pulse allows one to better utilize the IR-pumped Rydberg wavepacket, taking advantage of the focusing of the IR-driven wavepacket onto the parent ion [40] by soft scattering from the Coulomb potential. To aid the comparison to the results shown in figure 3, central XUV frequencies used in that figure are marked by the vertical lines. For longer XUV pulses, the dependence of XUV lasing on Ω_{XUV} follows the pattern seen in conjunction with figure 3: namely, XUV lasing occurs in the vicinity of the ionization threshold. It gradually decreases for increasing central XUV frequencies. Compared to figure 3, the gain is confined to a narrower range of central XUV frequencies due to the narrower spectral bandwidth of the longer XUV pulses for longer pulse lengths.

In the following, we will discuss several possibilities to increase the reported strong-field driven XUV amplification. One way is to increase the population of the IR-driven, quasi-bound continuum wavepacket taking explicit advantage of the stabilization of excited electronic states [31, 36–38]. Such additional pumping of excited electronic states might be provided e.g. by an external source [31], by the lower harmonics of the IR field generated in the medium or through collisional excitation at high particle densities. Figure 6(a) shows, using the parameters from figure 5, that a five-fold increase is achieved when the atomic medium is initially prepared in an excited state. Any excitation in the medium will therefore increase the gain, with the results of an initially unexcited sample giving the lower bound. Furthermore, as was stressed above, the ionization potential I_p plays a key role in the amplification mechanism: the quasi-bound excited states oscillate in the IR dressing field and are energetically shifted above the ionization threshold. XUV lasing occurrs at the falling edge of the IR pulse, enabling XUV amplification in the vicinity of the threshold.

Figure 6. Enhanced gain from excited atomic states. (a) Same as figure 5 for a sample of hydrogen atoms prepared in the $5p_0$ state. Positive (negative) cross sections correspond to loss (gain). For comparison, the central XUV frequencies used in figure 3 are marked by the vertical lines. The gain is enhanced by a factor of roughly five compared to an unexcited sample, figure 5. (b) Same as figure 6(a) for a sample of helium atoms, initially prepared in the 4s (blue), $5p_0$ (green) and $5d_0$ (red) states. Here, the intensity of the eight-cycle $\sin^2$ pulse is set to $I_{IR} = 9 \times 10^{15}$ W/cm^2, the time delay is set to $\Delta_{XUV} = -2.4$ fs and the duration of the XUV pulse is set to $T_{XUV} = 2.7$ fs. The respective ionization potentials are marked by the vertical black line.

Since the cross sections gradually decrease away from the ionization threshold (figures 3, 5, 6(a)), higher ionization potentials should therefore lead to the ability to amplify shorter wavelength. This is demonstrated in figure 6(b) for the example of helium atoms prepared initially in three different electronic states. We observe that in this system, both higher frequencies can be amplified and the overall absorption cross sections are higher than in hydrogen (see figure 6(a)). This is due to higher ionization potential and the higher photoionization cross sections in helium [41].

While the existence of quasi-bound, IR-driven excited states is the origin of the reported XUV lasing mechanism, their stabilization is nevertheless limited. Under the current conditions yielding simultaneous complete ground state depletion, most of the ionized electron density leaves the vicinity of the atom and is not amenable for amplification. Therefore, figure 7 explores the influence of a second center for enhanced amplification. Specifically, a doubly charged helium cation is placed at a distance of 10 bohr from the hydrogen atom. A short, intense ($I_{IR} = 9 \times 10^{14}$ W cm^{-2}) two-cycle IR driving field accelerates part of the electron density from the hydrogen to the He^{2+} site, see figure 7(a) for a plot of the electron density after the start of the simulation (0.05 fs) and after 2.4 fs. Shortly after the maximum of the two-cycle pulse at 2.1 fs, part of the electron density has been shot from the hydrogen to the He^{2+} site, enabling XUV stimulated recombination at the cation. Figure 7(b) shows the corresponding absorption cross sections, CS$_{XUV}(\Omega_{XUV})$, as function of the central XUV frequency Ω_{XUV} and of the IR driving field intensity. The time delay between the center of the XUV pulse and the maximum of the IR pulse is set to $\Delta_{XUV} = 0.25$ fs, see inset of figure 7(a). Strong XUV amplification is demonstrated in this model system in the range $\Omega_{XUV} = 60$–80 eV. With increasing IR driving field intensity, the IR driven electron gains more and more energy on its way from the hydrogen to the He^{2+} site, which is then converted into gain by the appropriately timed XUV pulse. In contrast to the amplification mechanisms in atoms (figures 1–6), amplification is possible in spite of the dominant electron localization at the hydrogen site (figure 7(a)). This is due to the different photoionization cross sections at the two sites, with the hydrogen atom being practically transparent for the high photon energies considered here.
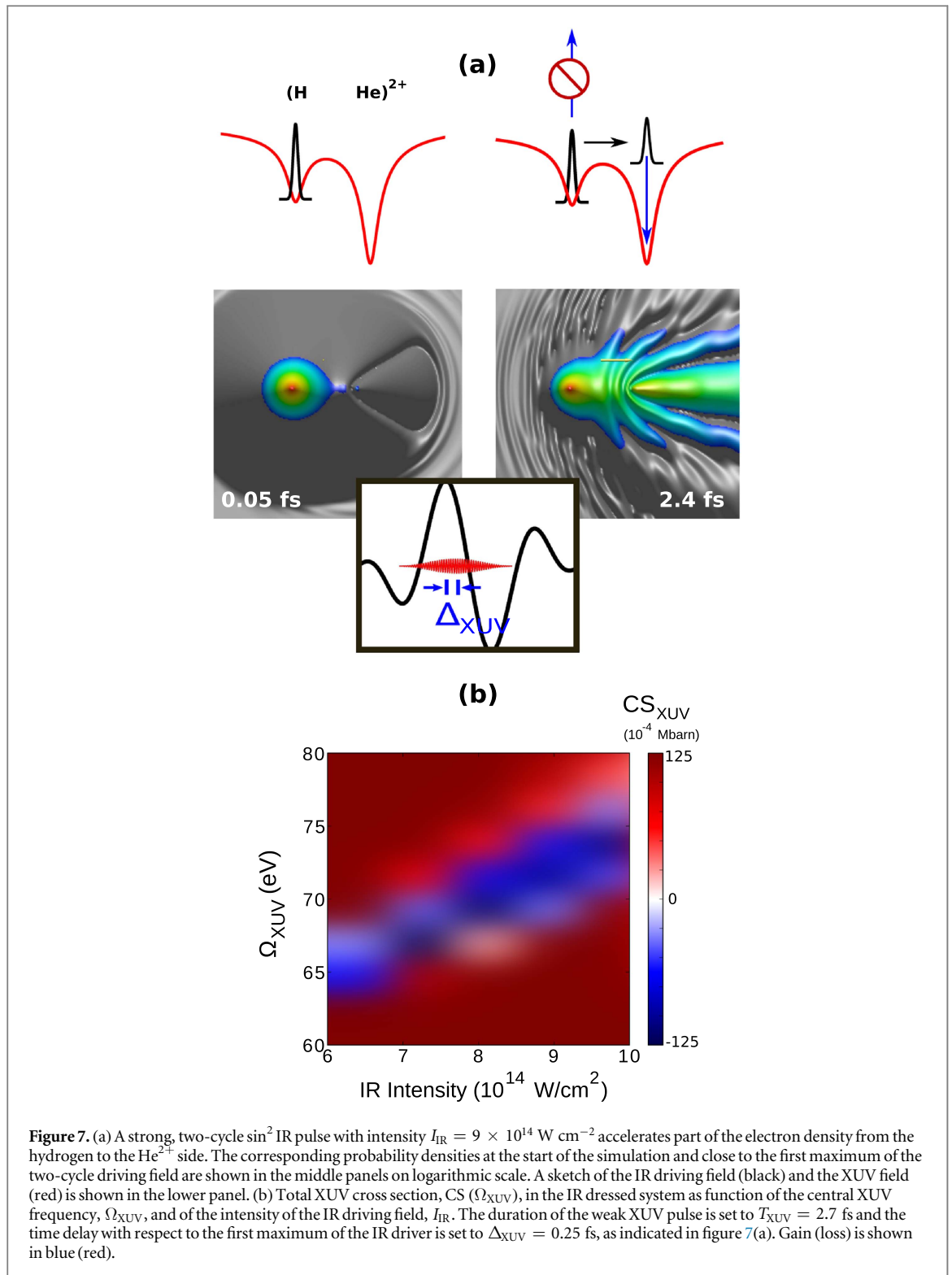
Figure 7. (a) A strong, two-cycle $\sin^2$ IR pulse with intensity $I_{IR} = 9 \times 10^{14}$ W cm^{-2} accelerates part of the electron density from the hydrogen to the He^{2+} side. The corresponding probability densities at the start of the simulation and close to the first maximum of the two-cycle driving field are shown in the middle panels on logarithmic scale. A sketch of the IR driving field (black) and the XUV field (red) is shown in the lower panel. (b) Total XUV cross section, CS (Ω_{XUV}), in the IR dressed system as function of the central XUV frequency, Ω_{XUV}, and of the intensity of the IR driving field, I_{IR}. The duration of the weak XUV pulse is set to $T_{XUV} = 2.7$ fs and the time delay with respect to the first maximum of the IR driver is set to $\Delta_{XUV} = 0.25$ fs, as indicated in figure 7(a). Gain (loss) is shown in blue (red).

Standard (parametric) HHG in such a multi-center setup has been the subject of numerous theoretical studies, investigating the possibility of the extension of the HHG cutoff in such a setup [42–44]. However, the experimental realization of such schemes is extremely hard due to the necessity for coherent delocalization of the electronic wavefunction between the multiple centers [44]. This requirement is absent in the present stimulated process. Moreover, analogous two center systems, i.e. neutral species (CH$_3$) dissociating from highly charged cations (I^{n+}) have already been prepared and demonstrated experimentally [45, 46]. Such species are also likely to occur in excited clusters [47].

4. Conclusions

We have, for the first time, identified a clear gain mechanism in HHG at the single atom level: the strong IR driving pulse creates an effective population inversion between the IR depleted ground state and the laser dressed excited states, enabling intra IR-pulse XUV lasing between such virtual states and the ground state. The former are populated by the frustrated tunneling mechanism [33–35]. For the hydrogen atom, our results are based on the numerically exact solution of the time-dependent Schrödinger equation, combined with a rigorous evaluation of the XUV absorption cross sections. As such, the simulations separate the facts from the fictions in the physics of stimulated HHG processes at the single atom level: any faithful theory must rigorously account for the loss channels in the medium, which, in our case, is one-photon XUV absorption from the ground state into the continuum (figure 1), see also [24]. This has not been accounted for at all previously [17–21].

While the strong field driven XUV gain is, at the single atom level, both weaker and only present at lower XUV energies as was reported in recent experiments [13–17], it is nevertheless a fact under suitable conditions. Our simulations show how, building up on this newly demonstrated mechanism, both the magnitude of the XUV gain and the energy of the amplified XUV radiation can be enhanced by orders of magnitude. Specifically, we establish a relation between the ionization potential of the gain medium and the range of XUV energies, for which amplification is possible (figures 3, 5, 6). Exploiting this relation, we demonstrate how gain media with higher ionization potential allow the amplification of shorter XUV wavelength (figure 6(b)). Furthermore, we show that any pre-excitation of the gain medium leads to a considerable increase of the gain (figure 6(a)).

While promising, the atomic amplification cross sections are nevertheless intrinsically limited by the wavepacket spreading. Also, the range of XUV energies where amplification is possible is limited to the vicinity of the ionization threshold. Our calculations on a model molecular system (figure 7) demonstrate that both restrictions can be relaxed in molecules or clusters.

Acknowledgment

References

[1] Krausz F and Ivanov M Y 2009 *Rev. Mod. Phys.* **81** 163
[2] Bredtmann T, Ivanov M Y and Dixit G 2014 *Nat. Commun.* **5** 5589
[3] Calegari F *et al* 2014 *Science* **346** 336
[4] Rundquist A, Durfee C G III, Chang Z, Herne C, Backus S, Murnane M M and Kapteyn H C 1998 *Science* **280** 1412
[5] Paul A, Bartels R A, Tobey R, Green H, Weiman S, Christov I P, Murnane M M, Kapteyn H C and Backus S 2003 *Nature* **421** 51
[6] Gibson E A *et al* 2003 *Science* **302** 95
[7] Zhang X, Lytle A L, Popmintchev T, Zhou X, Kapteyn H C, Murnane M M and Cohen O 2007 *Nat. Phys.* **3** 270
[8] Bandrauk A D and Shon N H 2002 *Phys. Rev.* A **66** 031401
[9] Takahashi E J, Kanai T, Ishikawa K L, Nabekawa Y and Midorikawa K 2007 *Phys. Rev. Lett.* **99** 053904
[10] Biegert J, Heinrich A, Hauri C P, Kornelis W, Schlup P, Anscombe M P, Gaarde M B, Schafer K J and Keller U 2006 *J. Mod. Opt.* **53** 87
[11] Brizuela F, Heyl C M, Rudawski P, Kroon D, Rading L, Dahlstrom J M, Mauritsson J, Johnsson P, Arnold C L and L'Huillier A 2013 *Sci. Rep.* **3** 1410
[12] Tudorovskaya M and Lein M 2014 *J. Mod. Opt.* **61** 845
[13] Seres J, Seres E, Hochhaus D, Ecker B, Zimmer D, Bagnoud V, Kuehl T and Spielmann C 2010 *Nat. Phys.* **6** 455
[14] Seres J, Seres E, Landgraf E, Ecker B, Aurand B, Kuehl T and Spielmann C 2014 *Sci. Rep.* **4** 4234
[15] Seres J, Seres E, Landgraf E, Ecker B, Aurand B, Hoffmann A, Winkler G, Namba S, Kuehl T and Spielmann C 2014 *Sci. Rep.* **4** 4254
[16] Dao L V, Dinh K B and Hannaford P 2015 *Nat. Commun.* **6** 7175
[17] Serrat C, Roca D, Budesca J M, Seres J, Seres E, Aurand B, Hoffmann A, Namba S, Kuehl T and Spielmann C 2016 *Opt. Express* **24** 8028
[18] Seres J, Seres E and Spielmann C 2012 *Phys. Rev.* A **86** 013822
[19] Serrat C 2013 *Phys. Rev. Lett.* **111** 133902
[20] Serrat C, Roca D and Seres J 2015 *Opt. Express* **23** 4867
[21] Serrat C 2016 *Phys. Rev.* A **93** 063415
[22] Kazamias S, Daboussi S, Guilbaud O, Cassou K, Montet C, Neveu O, Cros B, Ros D and Maynard G 2010 *Nat. Phys.* **6** 927
[23] Kazamias S, Daboussi S, Guilbaud O, Cassou K, Ros D, Cros B and Maynard G 2011 *Phys. Rev.* A **83** 063405
[24] Bredtmann T, Patchkovskii S and Ivanov M Y 2016 *Phys. Rev. Lett.* **117** 109401
[25] Mukamel S 1995 *Principles of Nonlinear Optical Spectroscopy* (Oxford: Oxford University Press)
[26] Patchkovskii S and Muller H G 2016 *Comput. Phys. Commun.* **199** 153
[27] Tong X M and Lin C D 2005 *J. Phys. B: At. Mol. Opt. Phys.* **38** 2593
[28] Smirnova O, Patchkovskii S and Spanner M 2007 *Phys. Rev. Lett.* **98** 123001
[29] Manolopoulos D 2002 *J. Chem. Phys.* **117** 9552
[30] Chelkowski S, Bredtmann T and Bandrauk A D 2013 *Phys. Rev.* A **88** 033423
[31] Bredtmann T, Chelkowski S, Bandrauk A D and Ivanov M Y 2016 *Phys. Rev.* A **93** 021402
[32] Wu M, Chen S, Schafer K J and Gaarde M B 2016 *J. Phys. B: At. Mol. Opt. Phys.* **49** 062003
[33] Nubbemeyer T, Gorling K, Saenz A, Eichmann U and Sandner W 2008 *Phys. Rev. Lett.* **101** 233001
[34] Eichmann U, Saenz A, Eilzer S, Nubbemeyer T and Sandner W 2013 *Phys. Rev. Lett.* **110** 203002

[35] Zimmermann H, Patchkovskii S, Ivanov M Y and Eichmann U 2016 *Phys. Rev. Lett.* **118** 013003
[36] Popov A M, Tikhonova O V and Volkova E A 2011 *J. Mod. Opt.* **58** 1195
[37] Morales F, Richter M, Patchkovskii S and Smirnova O 2011 *PNAS* **108** 2011
[38] Richter M, Patchkovskii S, Morales F, Smirnova O and Ivanov M Y 2013 *New J. Phys.* **15** 083012
[39] Bethe H A and Salpeter E E 1977 *Quantum Mechanics of One- and Two-Electron Atoms* (New York: Plenum)
[40] Yudin G L and Ivanov M Y 2001 *Phys. Rev. A* **63** 033404
[41] Marr G V and West J B 1976 *At. Data Nucl. Data Tables* **18** 497
[42] Moreno P, Plaja L and Roso L 1997 *Phys. Rev. A* **55** R1593
[43] Strelkov V V, Platonenko V T and Becker A 2005 *Phys. Rev. A* **71** 053808
[44] Lein M 2005 *Phys. Rev. A* **72** 053816
[45] Erk B *et al* 2014 *Science* **345** 288
[46] Boll R *et al* 2016 *Struct. Dyn.* **3** 043207
[47] Saalmann U, Siedschlag C and Rost J M 2006 *J. Phys. B: At. Mol. Opt. Phys.* **39** R39